

## Automated mapping of K-feldspar by electron backscatter diffraction and application to $^{40}\text{Ar}/^{39}\text{Ar}$ dating

Sandra McLaren<sup>a,\*</sup>, Steven M. Reddy<sup>b</sup>

<sup>a</sup> Research School of Earth Sciences, Australian National University, Acton, Australian Capital Territory 0200, Australia

<sup>b</sup> The Institute for Geoscience Research, Department of Applied Geology, Curtin University of Technology, GPO Box U1987, Perth, WA 6845, Australia

### ARTICLE INFO

#### Article history:

Received 16 October 2007

Received in revised form 15 May 2008

Accepted 30 May 2008

Available online 11 June 2008

#### Keywords:

Electron backscatter diffraction (EBSD)

Microstructure

Deformation

Thermochronology

Argon

Multidomain diffusion (MDD)

### ABSTRACT

The ability to quantify feldspar microstructure using the electron backscatter diffraction (EBSD) method has direct application in the study of rock deformation and strain kinematics. However, automated EBSD analysis of low symmetry phases, such as feldspar, has previously proven difficult. Here, we successfully apply the EBSD method to a number of granitic feldspars and develop automated phase and orientation mapping to discriminate K-feldspar and plagioclase, and quantify orientation variations within individual K-feldspar grains. These results represent the first automated quantitative mapping of orientation microstructure in K-feldspar. We use the method to evaluate the relationship between microstructure and  $^{40}\text{Ar}/^{39}\text{Ar}$  age, a controversial problem in thermochronology. In a granitic K-feldspar from central Australia, the range of observed orientation domains matches the small to intermediate and largest domain sizes predicted from multiple-diffusion domain modeling. In situ ultra-violet laser microprobe analyses show that the youngest ages from the  $^{40}\text{Ar}/^{39}\text{Ar}$  age spectra are recorded by grain mosaic K-feldspars with diameter around 10–50  $\mu\text{m}$ . These K-feldspars are the smallest coherent microstructural features observed on scales of  $>1 \mu\text{m}$ . Large 250–1000  $\mu\text{m}$  diameter microstructurally simple grains record the oldest ages observed in the age spectrum. These results suggest a first order relationship between K-feldspar microstructure and  $^{40}\text{Ar}/^{39}\text{Ar}$  age and demonstrate a microstructural control on multidomain diffusion.

© 2008 Elsevier Ltd. All rights reserved.

### 1. Introduction

Electron backscatter diffraction (EBSD) is a scanning electron microscope (SEM) technique that allows phase identification and the quantitative analysis of orientation variations in crystalline materials. The method utilizes diffraction of electrons by the crystalline lattice, which generates a number of bands (“Kikuchi” bands) that each corresponds to a set of lattice planes with a width that is directly related to lattice spacing (Randle, 2000). Together these bands form an electron backscatter diffraction pattern (EBSP) that is characteristic of both the phase and orientation of the crystal (e.g., Prior et al., 1999). By automatically collecting EBSPs over a predefined grid, EBSD data can be used to generate maps of phase and orientation data that allow the linkage of EBSD data to spatial position on a particular surface within the sample. Such an approach is performed on specially polished material surfaces and is non-destructive, allowing additional analytical techniques to be applied to the same sample. This approach therefore has certain

advantages over much higher spatial resolution transmission electron microscopy (TEM) for investigating the relationship between microstructure and geochemistry. Unlike transmission electron microscopy, EBSD analysis can also be coupled directly with orientation contrast imaging (Prior et al., 1996), providing constraints on the microstructural context.

EBSD analysis of high symmetry geological materials such as olivine (Faul and Fitz Gerald, 1999), garnet (Prior et al., 2002), calcite (Bestmann and Prior, 2003), galena (Skrotzki et al., 2000) and zircon (Reddy et al., 2007) has yielded useful insights into the microstructural behavior of these minerals during recrystallization, deformation and/or grain growth. However, EBSD analysis of lower symmetry phases, and particularly feldspars, has proven difficult. The reasons for this difficulty are the complex nature of feldspar EBSPs, the similarity of EBSPs between different feldspar phases, the various feldspar twin laws, pseudosymmetry in feldspars and problems associated with sample preparation. As a result automated EBSD analysis of feldspar has been difficult and the successful application of EBSD to feldspar (e.g. Prior and Wheeler, 1999; Jiang et al., 2000) has relied upon manual indexing of EBSPs, which is time consuming and does not readily permit the integration of geochemical data within a spatially-constrained microstructural context afforded by automated EBSD mapping.

\* Corresponding author. School of Earth Sciences, University of Melbourne, Elgin Street, Victoria 3010, Australia. Tel.: +61 3 8344 7675; fax: +61 3 8344 7761.

E-mail address: [mclarens@unimelb.edu.au](mailto:mclarens@unimelb.edu.au) (S. McLaren).

Here, we develop the use of automated EBSD mapping of alkali-feldspar in a variety of granitic rocks. We present a description of the method, operating conditions and indexing parameters employed. We then show the results of the automated EBSD mapping, including: (1) the successful discrimination of alkali-feldspar and coexisting plagioclase; and (2) the collection and analysis of quantitative crystallographic orientation data for K-feldspars.

We apply the EBSD method to the problem of linking quantitative orientation microstructure and  $^{40}\text{Ar}/^{39}\text{Ar}$  age in K-feldspars. The mineralogy of K-feldspar has been extensively studied and its use in thermometry (e.g. Elkins and Grove, 1990) and argon geochronology (e.g. Spell et al., 1996; Swisher et al., 1993; McDougall, 1985) is well established. However, the thermochronologic use of K-feldspar remains controversial. The multiple-diffusion domain (MDD) model (Lovera et al., 1989; Richter et al., 1991) attests that argon loss in K-feldspars is controlled only by thermally-activated volume diffusion and that the strong  $^{40}\text{Ar}/^{39}\text{Ar}$  age gradients often seen in K-feldspars are the result of variable argon retention by diffusion domains of different sizes (Lovera et al., 1989, 1991). The notion of a number of different sized diffusion domains comes largely from the characteristic non-linear Arrhenius behavior (Lovera et al., 1989). Individual diffusion domains are non-interacting and of simple geometry, and argon is lost instantaneously from domain boundaries. The fundamental tenet of the model is that the retention of argon during cooling in nature and the loss of argon during step-heating in the laboratory is controlled only by thermally-activated volume diffusion. The presence of a range of diffusion domain sizes yields a range in closure temperature that can be inverted to yield continuous cooling histories (Richter et al., 1991). As such, the method has become a potentially powerful tool in the reconstruction of exhumation histories and in the solution of various tectonic and structural geology problems (e.g. Dunlap and Fossen, 1998; McLaren et al., 2002) where it appears to give geologically reasonable cooling histories that are internally consistent and that are also consistent with apparent ages from higher and lower temperature chronometers, such as  $^{40}\text{Ar}/^{39}\text{Ar}$  muscovite ages and apatite fission track ages.

However, only about half of all the K-feldspars analysed are suitable for thermal history analysis (Lovera et al., 2002) and there is considerable controversy regarding the validity of the method. In particular: (1) Lee (1995) questioned the assumption that volume diffusion is the only mechanism of argon loss, arguing that fast-pathway diffusion can also influence the argon release; comparisons of UV laserprobe Argon data with qualitative analysis of deformation microstructure support this (Reddy et al., 2001); (2) Parsons et al. (1999) questioned the presence of a discrete domain structure with the specific characteristics required by the MDD model as well as the assertion that K-feldspar microstructures form only at temperatures above the closure temperature of diffusive argon loss; and (3) the role of sub-micron features such as micropores, subgrain boundaries and 'nanotunnels' remains unresolved (Fitz Gerald et al., 2006).

Central to all of these arguments is the question of how microstructure and argon loss are linked and to some extent this controversy reflects the inconsistency between the complex microstructural characteristics observed in K-feldspar and the relative simplicity of the MDD model. The work of Reddy et al. (2001) indicates that the way in which strain is accommodated within K-feldspar is a key control on the way in which the distribution of argon is modified. However, despite more than 20 years of work characterizing textural variations in K-feldspar, particularly at the sub-micron scale, there is still no explanation for the correlation between argon age and deformation-related microstructure reported by Reddy et al. (1999, 2001) other than the observation

that orientation domain boundaries facilitate the grain-scale redistribution of argon. To help resolve this problem it is essential to integrate quantitative analysis of intragrain orientation variations with thermochronologic data. We link orientation microstructure and  $^{40}\text{Ar}/^{39}\text{Ar}$  age by analysing the K-feldspar from a given sample using both  $^{40}\text{Ar}/^{39}\text{Ar}$  step-heating (on separated K-feldspar grains) and in situ  $^{40}\text{Ar}/^{39}\text{Ar}$  analysis (on individual K-feldspars in thin section). As such, this study builds on previous work investigating deformation-related subgrains and Ar isotope systematics (Reddy et al., 1999, 2001) by providing the first link between quantitative orientation data, derived by EBSD, and  $^{40}\text{Ar}/^{39}\text{Ar}$  ages.

## 2. Sample descriptions

Alkali-feldspar from three granitic sample suites was selected for this study. In all cases, macroscopically undeformed feldspars from undeformed granites were analysed to better enable results to be directly linked to samples typically used in the MDD approach. Compositionally, the analysed feldspars range from grains, which are obviously perthitic under the light microscope, to homogenous microcline or orthoclase grains.

### 2.1. Big Lake Suite granites, Warburton Basin, Australia

The Big Lake Suite granites are of Carboniferous age ( $323 \pm 5$  and  $298 \pm 4$  Ma; Gatehouse et al., 1995), and intrude the Warburton Basin at the base of the Cooper/Eromanga Basin in northern South Australia. The granites are compositionally and texturally complex and three samples exhibiting a variety of textural characteristics were chosen. These samples were obtained from core material extracted from three petroleum exploration wells; Sample 02-149 from a depth of 2895.2 m in Moomba-1; Sample 01-147 from a depth of 3056.7 m in Big Lake-1 and 02-152 from a depth of 3748.8 m in McLeod-1. Uncorrected temperatures in the granite range from 160 to 230 °C, and at least in part represent a recent increase in geothermal gradient associated with high temperature fluid-flow (McLaren and Dunlap, 2006). Sample 02-149, containing K-feldspar, plagioclase, quartz and biotite, is the most pristine of the three samples. In hand specimen it is characterized by classic igneous textures and highly lustrous euhedral crystal faces. Individual alkali-feldspar grains are coarsely perthitic, show good crystal shape, and an almost total absence of alteration features such as clay minerals or dissolution pits (McLaren and Dunlap, 2006). Sample 02-147 shows complex textural features on the scale of individual grains and also complex grain boundary zones; the feldspars are characterized by moderate development of 10–50 µm clay mineral laths and perthitic exsolution textures. In hand specimen the sample is characterized by sugary-textured opaque feldspar. The third sample (02-152) exhibited extremely complex textural features with feldspar grains characterized by large overgrowths of highly altered mica and clay minerals, probably as a result of extensive hydrothermal alteration and/or recrystallization. This sample was unable to be polished to sufficiently high quality for EBSD analysis to be performed.

The alkali-feldspars in all three samples are almost pure orthoclase containing only very minor amounts of Na (<1.6 wt%) and Ca (<0.04 wt%). The average of a number of point analyses give alkali-feldspar compositions in the range  $\text{An}_{0-0.1}\text{Ab}_{4.3-8.2}\text{Or}_{91.7-95.7}$  (Table 1). Coexisting plagioclase in perthitic exsolution lamellae is almost pure albite with a composition around  $\text{An}_{3.2}\text{Ab}_{95.5}\text{Or}_{1.3}$  (Table 1). The granites are inferred to have intruded during compression associated with the Alice Springs Orogeny (Sun, 1997) and the thermal conditions associated with this event in the region suggest that the granites are likely to be intermediate temperature melts, with crystallization temperatures ~700–750 °C (Sun, 1997; McLaren and Dunlap, 2006).

**Table 1**  
Electron microprobe point analyses for individual feldspars

	K <sub>2</sub> O	CaO	FeO	Fe <sub>2</sub> O <sub>3</sub>	BaO	Na <sub>2</sub> O	MgO	Al <sub>2</sub> O <sub>3</sub>	SiO <sub>2</sub>	Total	
Dead Fox Granite	11.3019	0.0154	Nd		0.3557	0.9459	0.0192	19.589	66.0658	98.2929	
	11.3413	0.037	Nd		0.3817	0.8926	0.0116	19.512	65.7536	97.9298	
	11.3434	0.033	0.0004		0.3600	0.9421	nd	19.8205	65.4977	97.997	
	11.3594	0.0252	0.0068		0.3855	0.9588	nd	19.7518	66.0949	98.5823	
	11.4921	0.0026	0.0081		0.3946	0.7647	nd	19.648	65.6808	97.9909	
	11.3449	0.0145	0.0039		0.3337	0.9814	nd	19.6819	66.6118	98.972	
	11.3196	0.0266	0.0184		0.3258	1.0306	nd	19.8531	65.8768	98.4508	
	11.3789	0.0197	0.0041		0.3226	0.9983	nd	19.449	65.648	97.8205	
01-524	12.0986	0.0219	nd		0.0871	0.3758	0.0054	19.8005	65.3104	97.6997	
	11.884	0.03	0.0313		0.0641	0.5131	0.0027	19.8104	64.1321	96.4677	
	12.2487	nd	0.0049		0.0307	0.2	0.0177	19.7974	64.5125	96.8119	
	12.2055	0.0148	nd		nd	0.3409	0.0041	19.8481	64.0276	96.441	
	11.8982	0.0405	0.0056		0.0103	0.4654	0.0095	20.1106	63.8367	96.377	
	12.0424	0.0412	0.0273		0.0116	0.4591	nd	20.0078	63.3243	95.9136	
	11.8492	0.0212	0.0188		nd	0.5267	0.0034	20.1366	63.0283	95.5842	
	11.9554	0.0188	0.0124		0.0077	0.4979	0.0116	20.1536	63.1732	95.8305	
	11.9908	0.02	0.009		0.0434	0.5026	nd	20.0731	63.1294	95.7682	
	12.1116	0.0121	0.0082		0.1279	0.3548	nd	19.9813	65.1167	97.7125	
	0.054	0.413	0.0155		nd	10.8763	0.0058	21.4695	67.9193	100.7534	
	0.0628	0.6001	0.1133		nd	10.7773	0.0044	21.4776	68.0796	101.1151	
	0.0675	0.9075	0.0148		nd	10.5686	nd	21.816	67.3763	100.7507	
	02-149	15.9772	0.0434		0.0756	0.0166	0.896		18.2477	64.3588	99.6152
16.3214		0.0176		0.0272	0.0277	0.6258		18.0662	64.3981	99.5737	
14.0948		0.023		0.0530	nd	1.6837		18.1095	64.2642	98.2282	
16.2271		0.0396		0.0212	0.0221	0.6378		18.2375	64.0496	99.2349	
16.8626		0.0159		0.0575	nd	0.2877		18.2839	64.3495	99.8911	
15.2475		0.0141		nd	0.0111	1.4299		18.1836	65.0951	99.9813	
15.5439		0.0293		0.0862	0.0498	1.1311		18.2912	64.0321	99.1635	
15.6341		0.0251		0.0650	0.0277	1.1512		18.31	63.7699	98.9892	
16.2978		0.019		nd	nd	0.4982		18.1694	64.0373	99.0217	
0.2609		1.6961		0.0852	nd	10.3391		21.0156	66.9047	100.321	
0.1954		0.0808		0.0107	0.0275	11.5064		19.2678	68.6355	99.7242	
0.2346		0.2131		0.0122	0.0771	11.1043		19.5654	68.4793	99.686	
02-147		13.873	0.0271		0.1686	0.0054	1.0334		18.7846	63.5762	97.4684
		15.0604	nd		0.0015	0.0654	1.3669		18.3029	61.1327	95.9298
	16.7583	0.0131		nd	nd	0.1932		18.3867	64.9228	100.2958	
	16.8522	nd		0.0333	0.0387	0.2471		18.5207	64.4575	100.1495	
	16.9467	0.0116		0.0119	0.1529	0.1832		18.792	63.441	99.5668	
	16.9883	nd		0.0149	nd	0.1797		18.3217	61.3782	96.9163	
	16.9924	0.0017		0.0179	0.1799	0.1658		18.2864	62.0894	97.7334	

## 2.2. Areyonga Formation boulder clast, central Australia

Sample 01-524 is a granitic boulder clast from the Areyonga Formation in the Amadeus Basin, central Australia. The Areyonga Formation is a Neoproterozoic (c. 720–660 Ma; Lindsay, 1989; Corsetti et al., 2006) diamicite conglomerate with calcareous and lithic sandstone interbeds all of glacial origin. The conglomeratic material is extremely poorly sorted and contains abundant sedimentary and basement-derived clasts. The sampled granitic boulder clast is spheroidal, ~40 cm in diameter, and exceptionally well preserved, containing abundant pink K-feldspar, quartz, plagioclase and biotite. In thin section the sample is characterized by typical igneous textures and the K-feldspars show no evidence for hydrothermal alteration or recrystallization. Around half of the feldspar grains are characterized by perthitic exsolution on scales of <1 μm to around 50 μm. The K-feldspar component is almost pure orthoclase with point analyses giving an average composition around An<sub>0.1</sub>Ab<sub>5.0</sub>Or<sub>94.8</sub> (Table 1). Coexisting plagioclase in exsolution lamellae is almost pure albite with point analyses giving a composition around An<sub>3.8</sub>Ab<sub>96.5</sub>Or<sub>0.6</sub> (Table 1). There is no evidence for deformation on the hand specimen or thin section scale.

## 2.3. Dead Fox Granite, central Australia

The Dead Fox Granite is late Palaeoproterozoic in age (Zircon <sup>207</sup>Pb/<sup>206</sup>Pb age = 1785 ± 4 Ma; Page, 1996) found in limited,

scattered outcrops between the Tanami and Arunta Inliers in central Australia. In hand specimen the sample contains distinctive large gray feldspar phenocrysts ranging from several millimeters to around 2 cm in diameter. The granite appears undeformed in hand specimen and thin section. The granite is part of Group 3 in the tripartite division of Australian Proterozoic igneous rocks of Budd et al. (2001). Petrogenetic considerations suggest that these rocks are the products of relatively high temperature melting around ~1000 °C as a result of melt-producing amphibole breakdown reactions.

In thin section, K-feldspar is associated with myrmekitic quartz and plagioclase in two main populations – coherent single grains (~350–1000 μm across) and disrupted grain mosaics (~20–50 μm). The large single K-feldspar grains are often surrounded by moats of K-feldspar-quartz-plagioclase myrmekite while the grain mosaic K-feldspars are themselves part of the myrmekitic texture, usually occurring on the margins of larger single K-feldspar, plagioclase or quartz grains (Fig. 1). Although models for the formation of myrmekite remain controversial, in the absence of evidence for deformation a symplectic crystallization model rather than a deformation-induced “myrmekitization” mechanism (e.g. Hippert and Valarelli, 1998) is inferred for the origin of the texture in the Dead Fox Granite. That is, the myrmekitic texture is considered to be the product of auto-metamorphic reactions occurring at relatively high temperatures during crystallization of the granite (e.g. Castle and Lindsley, 1993).

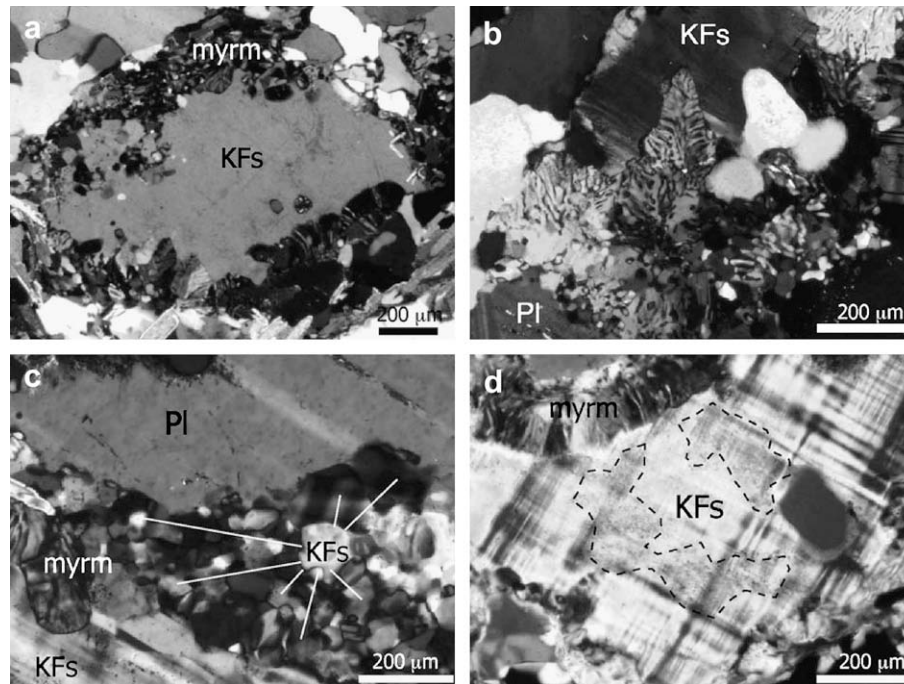


**Fig. 1.** Transmitted light micrographs of myrmekitic alkali-feldspar textures in the Dead Fox Granite (a) large single K-feldspar grain surrounded by moat of myrmekitic quartz, plagioclase and K-feldspar, (b) myrmekitic reaction front between K-feldspar and plagioclase grains, (c) similar view to (b) showing individual grain mosaic K-feldspars within the myrmekitic texture; (d) rare large K-feldspar grain showing well developed cross-hatched 'tartan' twinning; dashed lines outline regions of turbidity.

The composition of the K-feldspars is in the range  $An_{0.1}A-b_{11.2}Or_{88.7}$  (Table 1). Despite the relatively high Na content, the K-feldspars exhibit only very rare perthitic exsolution textures when viewed under the transmitted light microscope. Optical twinning is also rare and turbidity is variable (Fig. 1).

### 3. EBSD analysis

Petrographic thick (300 µm) sections of the granitic samples were prepared to allow the possibility of later  $^{40}Ar/^{39}Ar$  analysis using the ultra-violet laser microprobe. The sections were polished sequentially at different grades of abrasive down to 0.25 µm diamond paste, and subsequently prepared for EBSD analysis by chemical-mechanical polishing using a vibrating polyurethane lap and colloidal silica (0.06 µm in pH 10 NaOH) polishing fluid. Atomic number contrast (ANC) imaging using a backscatter detector, orientation contrast imaging using a forescatter detector (Prior et al., 1996) and EBSD analysis were all performed using a Philips XL30 Scanning Electron Microscope in the Microstructural Analysis Facility at Curtin University. To preserve the quality of the EBSD patterns, samples were not carbon-coated. Instead, samples were surrounded by carbon tape to reduce charging. An accelerating voltage of 20 kV, a working distance of 20 mm and sample tilt of 70° was used for all orientation contrast and EBSD analyses.

EBSD data were acquired and processed using Oxford Instruments/HKL Channel 5 software using the settings summarized in Table 2. Theoretical match units for a range of different feldspars were either derived from the HKL crystal files supplied with the EBSD system, the Mineralogical Society of America's Crystal Structure Database or utilizing the crystallographic and crystallochemical data obtained from the Mincrust database (Chichagov et al., 2001). Empirical testing of the different match units with the samples was undertaken to optimize the indexing process. This empirical testing, though less sophisticated than the approach of Reddy et al. (2008), showed that the best indexing was obtained

using monoclinic orthoclase ( $a = 0.8563$  nm,  $b = 1.2963$  nm,  $c = 0.7210$ ,  $\beta = 116.1^\circ$ ) and monoclinic albite ( $a = 0.8274$  nm,  $b = 1.2991$  nm,  $c = 0.7144$ ,  $\beta = 116.1^\circ$ ) structure data derived from Prince et al. (1973) and Winter et al. (1979), respectively.

For all data, the mean angular deviation (MAD) between the empirically obtained pattern and the theoretical solution was generally low (Table 2). MADs greater than 1.5° were rejected as poor quality fits at the indexing stage of data processing. Following standard EBSD procedures, all EBSD data were noise reduced using a "wildspike" correction to remove individual misindexed points

**Table 2**  
Settings for EBSD acquisition and processing

	EBSD settings		
	Fig. 3b–d	Fig. 4b–d	Fig. 5b–d
EBSP collection time (ms)	60	60	60
Background correction # frames	64	64	64
EBSP noise reduction			
– frames	4	4	4
– binning	4 × 4	4 × 4	4 × 4
– gain	Low	Low	Low
Band detection (min/max bands)	4/6	6/8	5/8
Hough resolution	65	60	65
MAD threshold	1.50	1.50	1.50
X steps	150	100	79
Y steps	144	100	81
Step distance (µm)	3	3	2
Cycling time (s/pattern)	0.263	0.280	0.315
Project duration	1:34:32	0:46:44	0:33:36
Zero solutions (%)	3.9	3.4	3.3
NR			
– 'wildspike'	Yes	Yes	Yes
– n neighbor zero solution	4	4	4
Albite %	27.7	39.2	15.0
Albite mean MAD	0.804	0.720	0.630
Orthoclase %	68.4	57.4	81.7
Orthoclase mean MAD	0.624	0.529	0.516

and a four-neighbor extrapolation to correct for some zero solutions (see Reddy et al., 2007 for details).

The EBSD data from each area were processed in different ways to produce a series of maps that show different aspects of the microstructure. Band contrast is a fundamental property of the EBSD that is obtained from the contrast identified in the Hough transform (Hough, 1962) used to recognize band edges in the EBSD and index to a theoretical feldspar diffraction pattern (or match unit). Band contrast is susceptible to variations in crystallographic orientation, structural integrity, crystal damage and surface topography and is therefore particularly useful for qualitatively delimiting sample microstructure independently of any data processing. Band contrast maps were therefore used as a background over which phase or orientation data were draped. Phase maps were produced by assigning a different color to each identified feldspar phase. Orientation maps were produced using a 'texture' component in which each pixel is colored for minimum misorientation relative to a user-defined reference orientation from a particular EBSD selected on the map.

Crystallographic orientation data were plotted using Channel 5 Mambo software using lower hemisphere, equal area projections. All data are reported with respect to an arbitrarily assigned X–Y coordinate framework for the sample surface. This permits intra sample orientation variations to be investigated and only precludes linkage of these variations to a field coordinate system (e.g. geographical coordinates).

#### 4. Discrimination of K-feldspar and plagioclase using automatic mapping

The successful discrimination of K-feldspar and plagioclase by EBSD is essential if the crystallographic orientation variation within individual feldspars is to be accurately quantified. The EBSDs obtained from the K-feldspar host and the associated perthitic plagioclase are very similar (Fig. 2), showing crystallographic orientations that are consistent with the established crystallographic

relationships between these phases. Despite this similarity, automatic EBSD mapping was able to effectively discriminate between K-feldspar and plagioclase (Fig. 3a,c, 4a,c and 5a,c) and shows that alkali-feldspars from the Big Lake Suite granite and the Areyonga Formation show some degree of perthitic exsolution at scales of  $<1\ \mu\text{m}$  to c.  $40\text{--}50\ \mu\text{m}$  (Figs. 3a, 4a and 5a). Two problems were encountered associated with phase misidentification. The first resulted in plagioclase EBSDs from a single area being systematically indexed as K-feldspar and is likely the result of automatic band selection not recognizing or using critical discriminating bands. The second arises from apparent misindexing of individual EBSDs within areas comprising only K-feldspar, as identified by ANC imaging. The resulting "checkerboard" pattern is a typical characteristic of misindexing of phases or pseudosymmetry relationships in individual phases. However, compositional information in K-feldspar rich areas indicates an abundance of  $<3\ \mu\text{m}$  cryptoperthite areas. Since these are smaller than the grid spacing of EBSD collection, many of the isolated analyses of plagioclase may be real rather than representing compositional misindexing (Figs. 3 and 4). The apparent misindexing is therefore partly a function of mapping resolution.

#### 5. Quantifying crystallographic orientations in K-feldspar

Macroscopically undeformed feldspar phenocrysts from undeformed granitic protoliths show considerable intragranular orientation variations. Individual grains of alkali-feldspar from a granitic boulder clast from the Areyonga Formation (Fig. 3) record internal variations up to  $17^\circ$  that are accommodated by the formation of discrete low-angle boundaries within the feldspar. These low-angle boundaries form traces oriented in two directions at approximately  $45^\circ$  to the arbitrarily defined sample X–Y axes (Fig. 3d). The interaction of these two directions results in orientation domains from 10 to  $100\ \mu\text{m}$  scale. The first of the boundary directions correspond to lines approximately parallel to (100) (Fig. 3e), although the similarity to the trace of perthitic exsolution

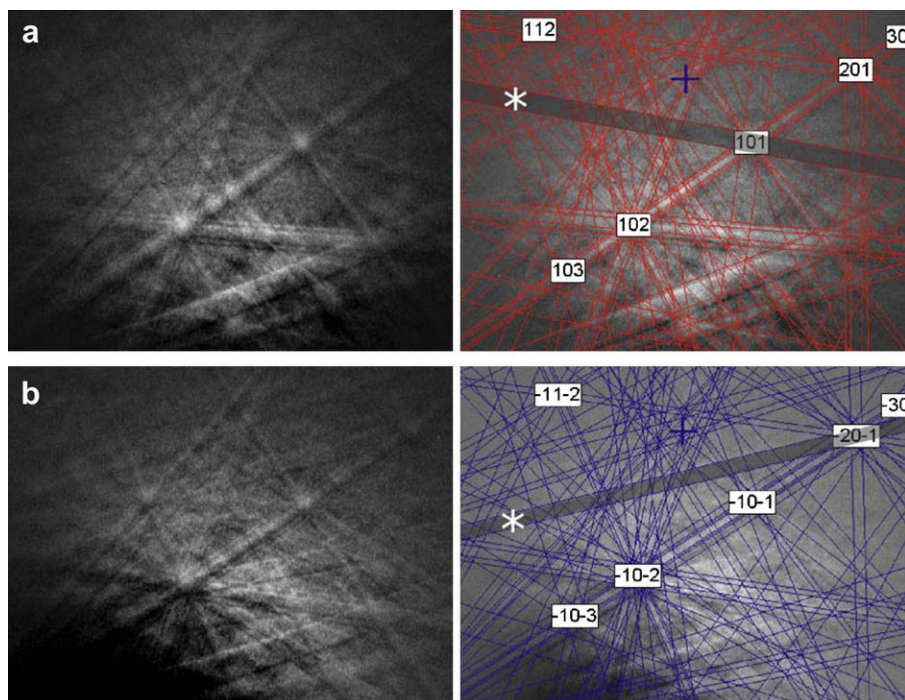


**Fig. 2.** Examples of empirically obtained electron backscatter patterns (EBSPs) together with the fit to theoretical reflector files (draped over the original EBSP) for (a) K-feldspar and (b) Plagioclase. Two diagnostic bands that allow the patterns to be discriminated are highlighted.

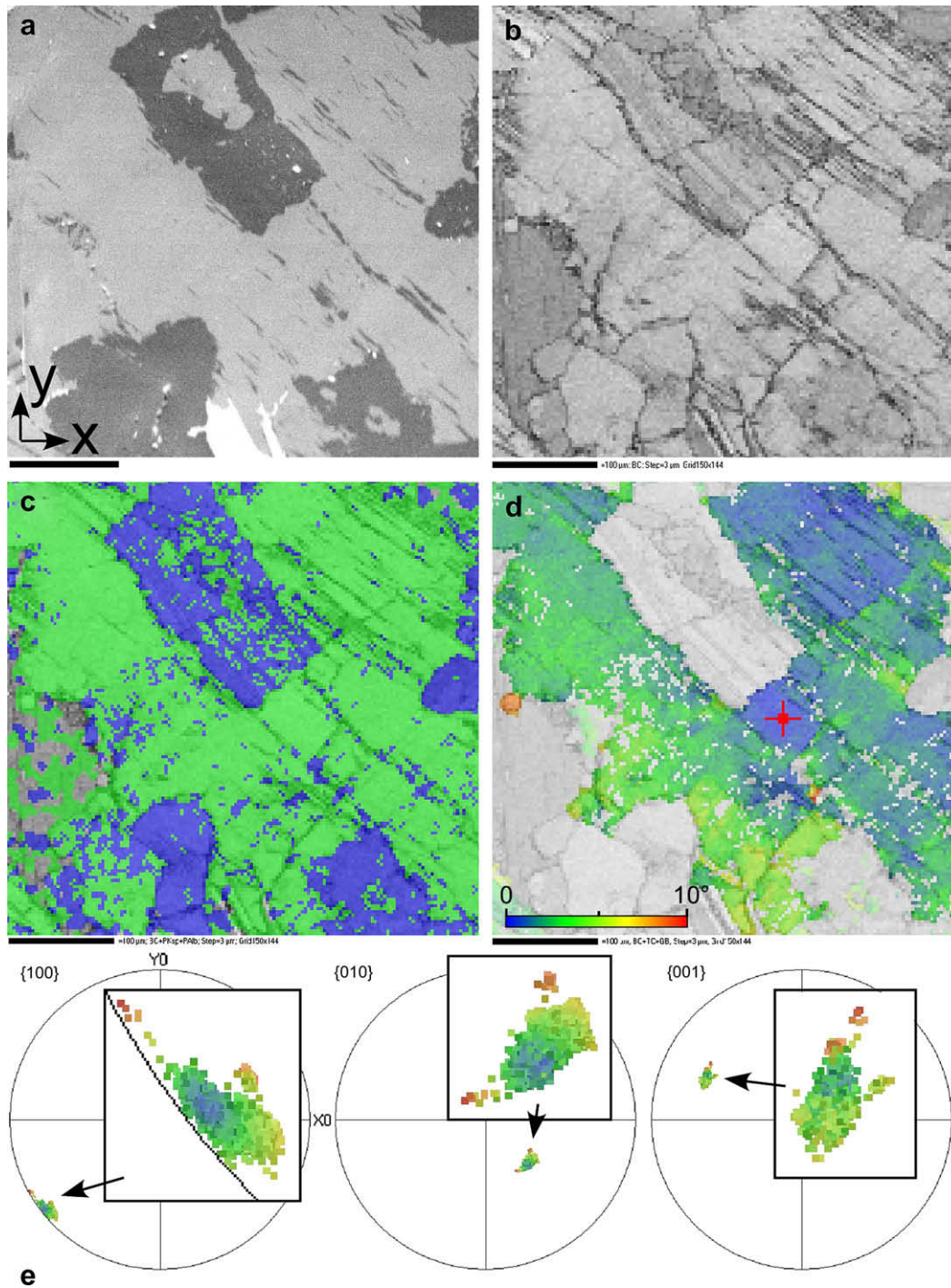


**Fig. 3.** Example of EBSD results from Sample 01-524, Areyonga Formation granitic K-feldspar, (a) gray scale ANC image (dark gray = plagioclase, light gray = K-feldspar), (b) band contrast image indicating the quality of the data points (c) electron backscatter diffraction phase map showing indexing of plagioclase (blue) and K-feldspar (green) via automatic mapping, (d) texture map showing a  $10^\circ$  misorientation variation, shown by the color bar, from the EBSD collected at the position of the red cross., (e) Lower hemisphere equal area projections of {100}, {010} and {001} crystallographic poles for data shown in (d). Data show total misorientation across the mapped part of the grain of  $17^\circ$ . Colors correspond to those shown in (d).

(Fig. 3a) indicates that the plane is probably  $\bar{6}01$ , the plane of minimum strain between two different monoclinic feldspars (Williams and Brown, 1974). The second direction is coincident with lines of low band contrast (Fig. 3b) that have traces approximately  $90^\circ$  to perthitic exsolution traces. The similarity of {100}, {010} and {001} within the grain indicate that these boundaries are not likely to represent twin planes. They could represent {010} and {001} cleavage planes, but with no constraints on the three dimensional geometry of the boundaries this is not possible to verify.

Feldspars from the Big Lake Suite granite (Figs. 4 and 5) record less orientation variations and do not show the discrete low-angle boundaries that characterize the Areyonga Formation sample. Instead the grains show gradual changes in orientation of c.  $1^\circ/100 \mu\text{m}$  (Figs. 4d and 5d). Such variations are not consistent with common feldspar features such as twinning and cleavage and are interpreted to reflect the accumulation of dislocations within the feldspars. Since the samples are macroscopically undeformed, the strain accommodated by these dislocations is interpreted to

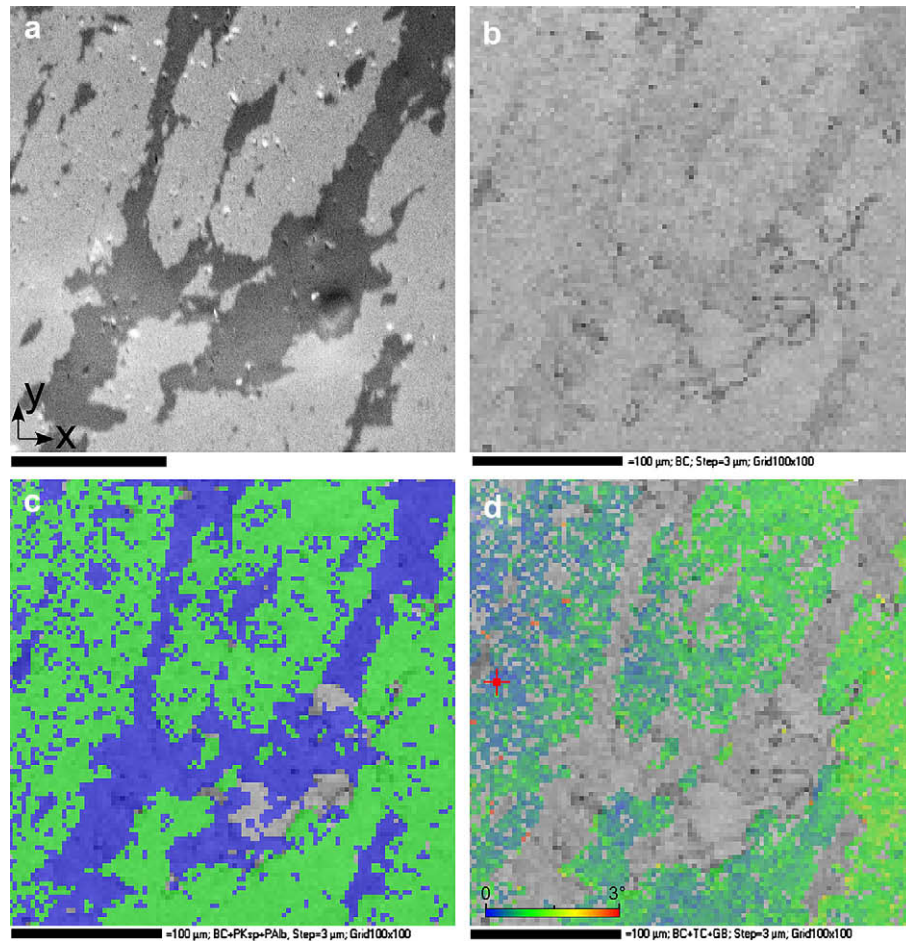


**Fig. 4.** Example of EBSD results from Sample 02-149, Big Lake Suite granitic K-feldspar. (a) gray scale ANC image (dark gray = plagioclase, light gray = K-feldspar), (b) band contrast image (c) electron backscatter diffraction phase map showing indexing of plagioclase (blue) and K-feldspar (green) via automatic mapping, (d) texture map showing a 3° misorientation variation, shown by the color bar, from the EBSD collected at the position of the red cross.

represent the response of the feldspar to thermal stresses during subsolidus cooling.

## 6. Application to $^{40}\text{Ar}/^{39}\text{Ar}$ thermochronology

Previous studies have attempted to address the issue of argon diffusion in K-feldspars, and particularly the relationship between microstructure and  $^{40}\text{Ar}/^{39}\text{Ar}$  ages. For example, Wartho et al. (1999) report a laser ablation microprobe study of the Benson Mines Orthoclase, a gem-quality K-feldspar characterized by very simple microstructure, and Fitz Gerald and Harrison (1993) report a detailed light microscopy and TEM study of K-feldspar MH-10, a sample well characterized by step-heating and MDD modeling. Only Reddy et al. (2001) have attempted to link  $^{40}\text{Ar}/^{39}\text{Ar}$  ages directly to microstructural observations at a high spatial resolution by: (1) determining  $^{40}\text{Ar}/^{39}\text{Ar}$  ages on a single K-feldspar grain using both step-heating and a high spatial resolution ultra-violet laser microprobe; and (2) characterizing the deformation-related microstructures in the same grain using orientation contrast imaging. However, quantitative orientation data was not included in this previous work and the success of the EBSD method documented here has the potential to provide extra constraints on this problem.

Of the samples subject to EBSD analysis, only feldspar from the Dead Fox Granite was subject to detailed in situ  $^{40}\text{Ar}/^{39}\text{Ar}$  analysis. This sample was chosen on the basis of: (1) its large range in recorded  $^{40}\text{Ar}/^{39}\text{Ar}$  ages from  $\sim 700$  to  $\sim 1550$  Ma; and (2) its

generally old ages (Fig. 6). Unfortunately, we are unable to link the microstructures identified in the other alkali-feldspar samples with their argon ages as the generally young ages of these grains ( $< 600$  Ma) mean that we could not precisely resolve ages of individual orientation domains using existing analytical facilities.

### 6.1. Furnace $^{40}\text{Ar}/^{39}\text{Ar}$ step-heating

The age spectrum of K-feldspar from the Dead Fox Granite is characterized by ages that increase, essentially monotonically, as temperature is raised (Fig. 6; Appendix). The first 20% of the gas release appears to be contaminated, as indicated by the large difference in the age of isothermal steps. This pattern is characteristic of excess argon associated with the decrepitation of Cl-rich fluid inclusions (Burgess et al., 1992; Harrison et al., 1994). The oldest age recorded in the age spectrum ( $1547 \pm 33$  Ma; Fig. 6) is  $\sim 200$  Ma younger than the intrusion age of the granite. This suggests that the granite has experienced post-intrusion heating, probably during the regional 1590–1560 Ma Chewings Orogeny (e.g., Teyssier et al., 1988; Hand and Buick, 2001). However, the absence of evidence for deformation and/or recrystallization suggests that the granite did not experience any deformation or metamorphism during this event, or at any other time following its intrusion. As discussed in Section 2, in the absence of evidence for deformation or recrystallization we consider the myrmekitic textures to have formed at temperatures only just below the solidus temperature, such that all of the observed microstructural features formed well above the

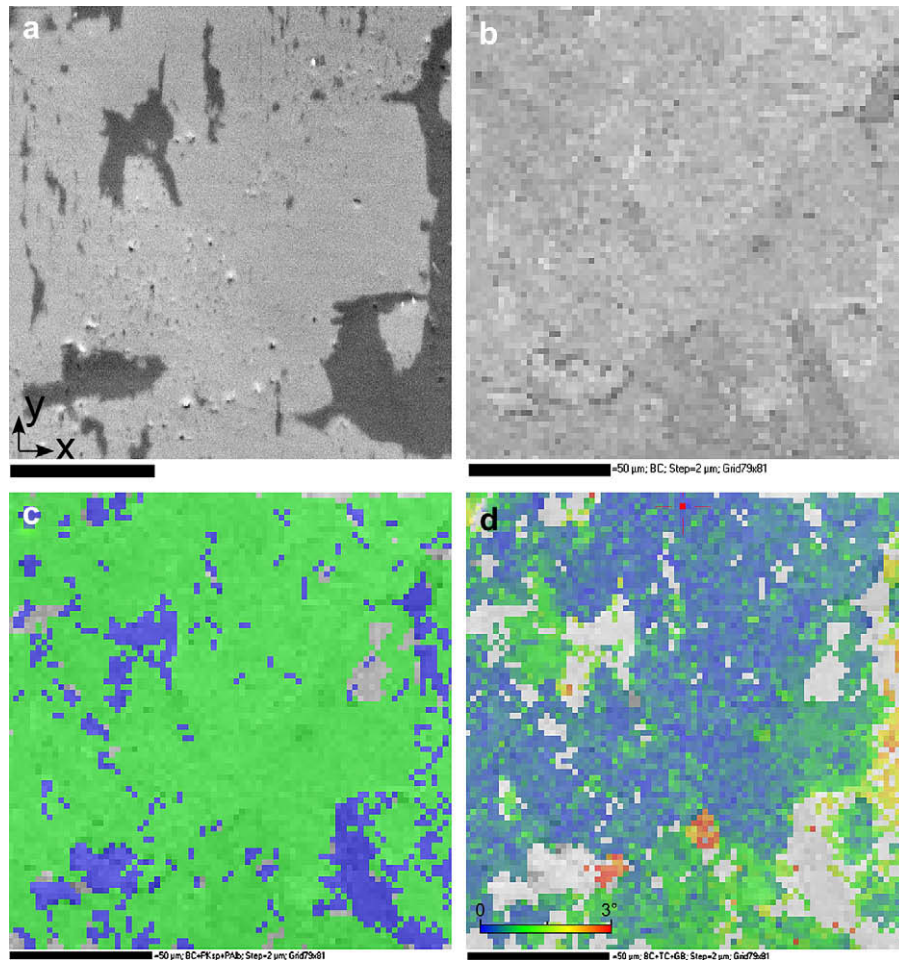


**Fig. 5.** Example of EBSD results from Sample 02-149, Big Lake Suite granitic K-feldspar. (a) gray scale ANC image (dark gray = plagioclase, light gray = K-feldspar), (b) band contrast image (c) electron backscatter diffraction phase map, showing indexing of plagioclase (blue) and K-feldspar (green) via automatic mapping, (d) texture map showing a 3° misorientation variation, shown by the color bar, from the EBSD collected at the position of the red cross.

accepted maximum closure temperature for argon loss ( $\sim 350$ – $400$  °C).

## 6.2. MDD modeling

The Dead Fox K-feldspar does not show any of the characteristics that may prohibit the successful application of the MDD model, such as excessive low temperature and/or high temperature excess argon, or intermediate age maxima (Lovera et al., 2002). Moreover, there is a very good correlation between the age spectrum and the calculated  $\log(r/r_0)$  plot (Fig. 7), a comparison with which we are able to assess the degree to which the age spectra and  $^{39}\text{Ar}$  release spectra are compatible with volume diffusion (Lovera et al., 2002). Note that the  $\log(r/r_0)$  plot is a representation of the domain size distribution relative to the volume fraction of  $^{39}\text{Ar}$  released (Lovera et al., 1991). The y-axis,  $\log(r/r_0)$ , represents the size of the domains contributing  $^{39}\text{Ar}$  at each stage in the experiment, relative to the reference length scale,  $r_0$ , defined from the initial gas release to which all domains contribute. The calculated correlation coefficient ( $C_{\text{fig}}$ ) between the age spectrum and the  $\log(r/r_0)$  plot, as defined by Lovera et al. (2002), is high at 0.95. Together these observations suggest that the MDD method may be appropriately applied to this sample.

The model produces a good fit to the laboratory Arrhenius and  $\log(r/r_0)$  data and the resultant thermal history produces a good fit to the laboratory age spectrum (Fig. 7). The activation energy ( $E_a$ ) is

calculated using the initial low temperature gas release, as defined by the linear portion of the Arrhenius array (Fig. 7b). The activation energy of 58 kcal/mol calculated for Dead Fox K-feldspar is high compared to the global average K-feldspar value of  $46 \pm 6$  kcal/mol, however it is still within the range for K-feldspar of  $\sim 30$ – $70$  kcal/mol reported by Lovera et al. (1997). We suggest this value is representative given that there is no evidence for contamination of the mineral separate and that repeat diffusion experiments on different aliquots and all give  $E_a = 58 \pm 2$  kcal/mol.

The resultant thermal history modeling gives a family of possible temperature-time paths (Fig. 7) that appear plausible given constraints on the regional tectonic and thermal histories available from the nearby Arunta and Tanami Inliers. The modeled thermal history predicts three major periods of cooling: (1) rapid cooling from around 1580 until 1500 Ma; (2) cooling between  $\sim 1000$  and 850 Ma; and (3) final cooling between 800 and 450 Ma. The exact timing of final cooling cannot be determined due to the excess argon contamination of the early released gas. Cooling between around 1580 and 1500 Ma is consistent with the known age of the Chewings Orogeny. Cooling commencing just prior to 1000 Ma may be associated with unroofing due to extension associated with the intrusion of the Stuart and Kulgera Dyke swarms (e.g., Zhao and McCulloch, 1993) immediately prior to the formation of the Centralian Superbasin (Walter et al., 1995). Although we are unable to constrain the timing of cooling precisely from this sample alone, we note that a similar record of cooling in the interval 1000–800 Ma is



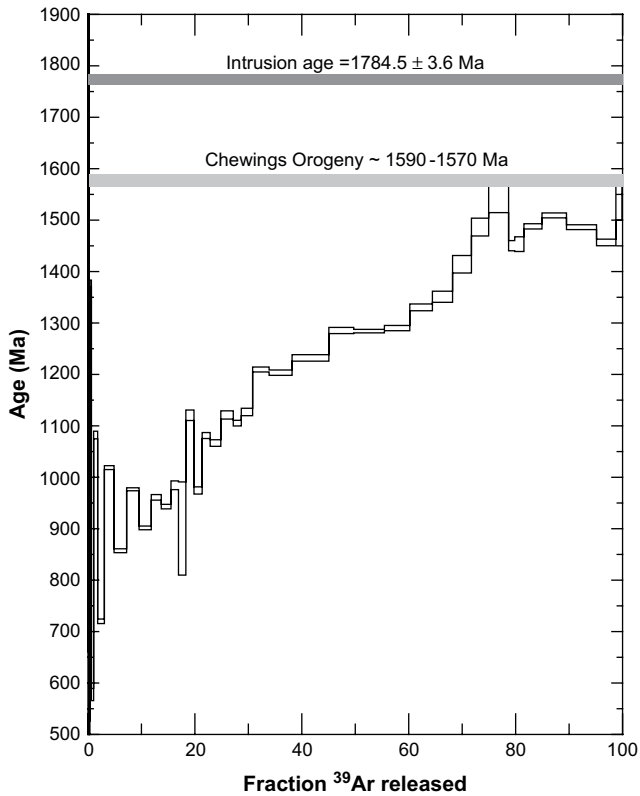


**Fig. 6.** Measured  $^{40}\text{Ar}/^{39}\text{Ar}$  age spectrum for K-feldspar from the Dead Fox Granite. Also indicated are the intrusion age (Zircon  $^{207}\text{Pb}/^{206}\text{Pb}$  age) and the approximate age of the Chewings Orogeny (Teyssier et al., 1988; Hand and Buick, 2001).

apparently recorded by a number of other K-feldspars from northern central Australia (S. McLaren, G. Fraser, unpublished data).

The MDD modeling makes predictions about the size of “domains” and the volume fractions of argon they contain from the

nature of the  $^{39}\text{Ar}$  release pattern (Fig. 7; Table 3). The automated MDD modeling routines can produce a set of up to 10 different domain distributions which, for the Dead Fox K-feldspar, each provide slightly different fits to the observed Arrhenius and  $\log(r/r_0)$  data. Lovera et al. (1991) have shown that although the release of  $^{39}\text{Ar}$  during step-heating does not allow the domain distribution to be determined uniquely, differences in the number of domains or their geometry do not significantly affect the modeled thermal history. For our purposes however, we are interested in at least the range of size and volume fraction of the predicted domain distribution. In our discussion we only include results from the peak best-fit solution (Table 3), which, based on the fits to the laboratory data, is considered to provide the best description of the domain structure.

The predicted domain distribution comprises eight domains that vary in size by a factor of 1800. However, as they are very similar in size, domains 3 and 4, and 5 and 6 can be combined without any degradation of the model result, meaning that our distribution contains only six distinct domain sizes (Table 3). A key feature of this simplified six-domain distribution is the presence of two domains, which we label C and F, and which together account for more than 60% of the total gas release (Table 3). Domain F is the largest domain size in the sample (relative domain size = 1.0) and contains ~23% of the total gas released. Domain C, the smaller of the two dominant domains is around 1/17th of the size of Domain F and contains almost 41% of the total gas released. The smallest domains (relative size = 0.00055 and 0.0023) together contain ~16% of the total gas and the remaining 21% of the gas released is predicted to have come from two intermediate sized domains with relative sizes ~0.21 and 0.31.

### 6.3. In situ UV $^{40}\text{Ar}/^{39}\text{Ar}$ dating

We have attempted to link the ages recorded in the age spectrum to the microstructural domains characterized by orientation variations using the ultra-violet laser ablation microprobe. The

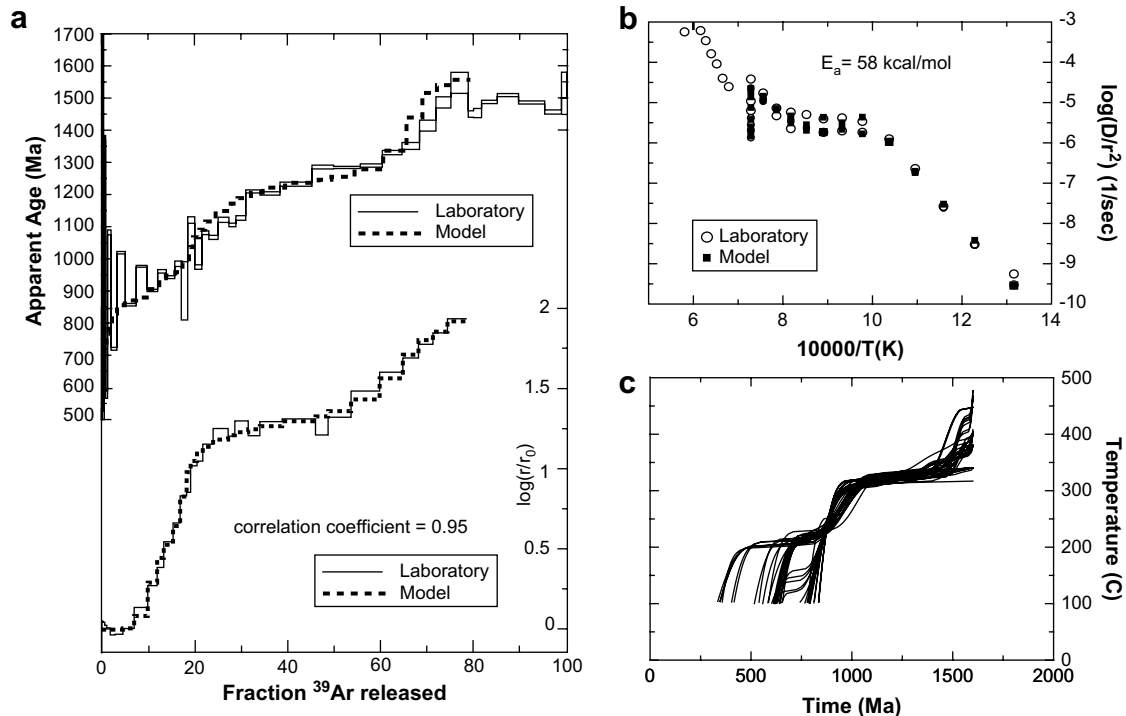


**Fig. 7.** Results of multiple-diffusion domain modeling (a) measured and modeled age spectra (b)  $\log r/r_0$  plots (c) measured and modeled Arrhenius data (d) preferred thermal histories.

**Table 3**  
Calculated domain distribution for Dead Fox Granite K-feldspar

Domain	Log Do cm <sup>2</sup> s <sup>-1</sup>	Volume fraction (%) $\phi_j$	Domain size (relative) $\rho_j$	Simplified domain distribution
1	9.31640	8.630	0.00055	A
2	8.08063	7.114	0.00230	B
3	5.24300	24.050	0.06026	C
4	5.22013	16.852	0.06187	
5	4.16447	11.811	0.20859	D
6	4.14975	6.645	0.21216	
7	3.83160	2.311	0.30601	E
8	2.80306	22.588	1.00000	F

primary drawback of in situ  $^{40}\text{Ar}/^{39}\text{Ar}$  analysis using UV laser heating is the preferential loss of excess argon from defects, dislocations and the decrepitation of fluid inclusions (e.g. Burgess et al., 1992; Mulch et al., 2002). We experienced some problems with excess argon contamination leading to artificially old ages in excess of the intrusive age of the granite. However, we were able to successfully obtain ages that were not obviously contaminated by excess argon that is, ages within the range recorded in the age spectrum (Figs. 8 and 9). Partly as a result of the problems we encountered with excess argon contamination, we were particularly interested in identifying candidate microstructural domains to account for the youngest and oldest ages recorded.

Sub-micron scale features that we could not characterize using the EBSD method, and for which we cannot obtain age information, are likely candidates for the smallest domains in the model domain distribution (with relative size 0.00055–0.0023 in this example). The relative size of these features is probably related to crystallographic structure and, as such, are likely to be similar to those

previously characterized by transmission electron microscopy in other samples (e.g. Fitz Gerald and Harrison, 1993).

Our microstructural observations suggest that the grain mosaic K-feldspars (as described in Section 2.3) are the next smallest coherent “domain” candidate that we can observe on a scale  $>1\ \mu\text{m}$ . These grain mosaic textured K-feldspars vary in diameter from around 20–50  $\mu\text{m}$  (Fig. 8). Fig. 8 shows the location and size of the ablation pits and  $^{40}\text{Ar}/^{39}\text{Ar}$  ages for these analyses, together with the EBSD orientation contrast images. The youngest ages recorded are  $701 \pm 168$ ,  $791 \pm 180$  and  $815 \pm 175$  Ma, which are all within error of one another and which correspond well to the youngest ages recorded in the age spectrum (Fig. 8). The large errors on the ages are largely attributable to the very small volumes of gas released. However, at least two of the ablation pits appear to sample smaller K-feldspar grains around 5  $\mu\text{m}$  in diameter with significant internal orientation contrast and which may represent more than one age domain, with the smaller sub-domains possibly characterized by even younger ages. The sampling of multiple age domains in this way may also help to account for the relatively high uncertainty on these ages.

In contrast to the young ages recorded by the small grain mosaic K-feldspars, large homogeneous regions of K-feldspar with apparently simple microstructure appear to record old ages ( $1569 \pm 18$  and  $1465 \pm 18$  Ma) that correspond well with the oldest ages recorded by the age spectrum (Fig. 9). These analyses suggest that in otherwise homogeneous K-feldspar, regions of pristine and turbid material are not characterized by significant differences in  $^{40}\text{Ar}/^{39}\text{Ar}$  age. This observation is at least consistent with the model of turbid K-feldspar forming under high-intermediate temperature conditions (around 450 °C; Parsons and Brown, 1984), above the closure temperature of K-feldspar to argon loss. However, we recognize that

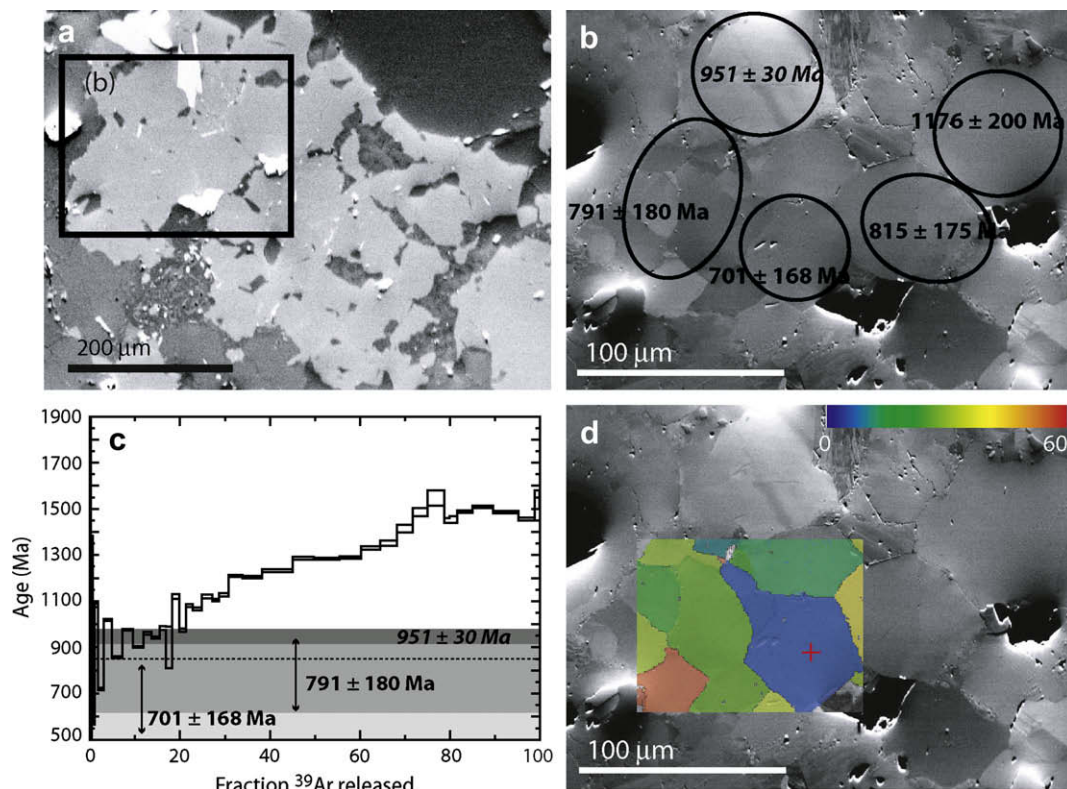


**Fig. 8.** Dead Fox Granite (a) back scattered electron image showing atomic number contrast; note disrupted microstructures associated with myrmekitic intergrowths of K-feldspar, quartz and plagioclase; box shows location of (b); (b) Orientation contrast image showing coherent subgrain K-feldspar, subgrains range in size from  $\sim 15$  to  $60\ \mu\text{m}$  and show little internal orientation contrast. Circles show the location and size of UV laser ablation pits and corresponding  $^{40}\text{Ar}/^{39}\text{Ar}$  ages; (c) age spectrum from grain separate showing ages, with one sigma errors, recorded by the three youngest spot analyses; (d) Orientation contrast image with EBSD map overlain. EBSD map shows texture component and is shaded red-blue to represent a  $60^\circ$  orientation contrast from pixel indicated by the red cross.

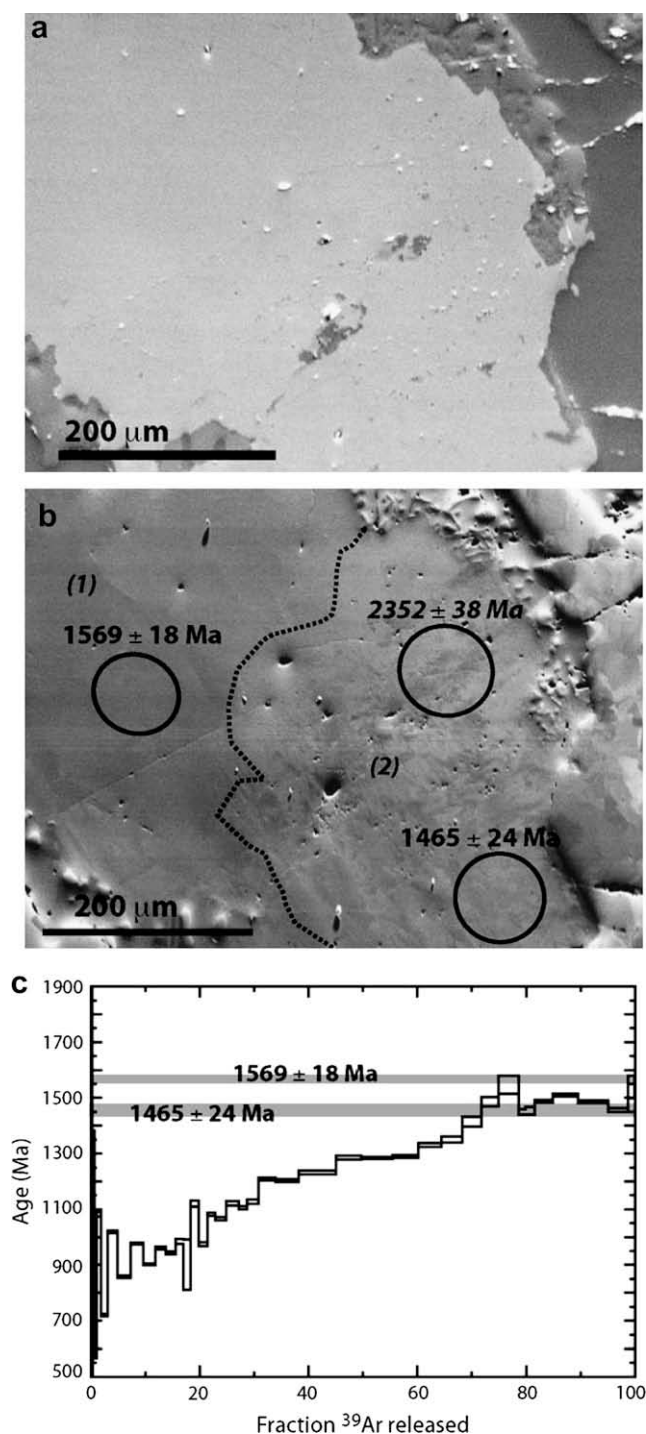


**Fig. 9.** Dead Fox Granite (a) ANC image showing atomic number contrast; (b) Orientation contrast image showing (1) area of macroscopically homogeneous K-feldspar characterized by only very subtle orientation contrasts and (2) area of turbid K-feldspar, characterized by small pits and holes and significant micron scale orientation contrast. Also shown are the location of the UV laser ablation pits and corresponding  $^{40}\text{Ar}/^{39}\text{Ar}$  ages; (c) age spectrum from grain separate showing actual ages recorded by the two spot analyses; age of  $2352 \pm 38$  Ma is older than the age of the granite and represents excess argon contamination.

even though these ages do correspond to the oldest ages in the age spectrum, in reality the true gas age may be younger and the ages we have measured could be contaminated by some (small) component of older excess argon. In the case of the Dead Fox Granite K-feldspars, very low total yield of  $^{37}\text{Ar}$  and  $^{38}\text{Ar}$  does not allow correction for chlorine-derived excess argon. Unfortunately this

inability to identify and/or correct for excess argon from individual laser ablation microprobe  $^{40}\text{Ar}/^{39}\text{Ar}$  analyses will also affect any future attempts at high resolution dating of K-feldspars in this way.

## 7. Discussion

We have shown that automated electron backscatter diffraction analysis can be successfully applied to K-feldspar. Appropriate choice of indexing parameters reduces misindexing problems and allows the successful discrimination of coexisting K-feldspar and plagioclase, despite the similarity of their electron-back-scattered patterns. Quantitative crystallographic orientation data allows misorientations to be quantified, revealing complex microstructural relationships even in undeformed K-feldspars. Although in this study we have focused on macroscopically undeformed samples, the technique should be applicable to all feldspars and is likely to be potentially useful in the analysis of deformation fabrics. Analysis of the deformation-related microstructure of feldspar using EBSD has a number of benefits over other methods. In particular, the EBSD method allows deformation-related microstructure to be characterized and quantified on a large range of scales, in contrast to TEM that can only resolve sub-micron scale variations in crystallographic orientation. The EBSD method also compares favorably to the method proposed by Waldron et al., 1994 in which cleavage surfaces of feldspars are etched using dilute hydrofluoric acid and then viewed under the scanning electron microscope. The etching method reveals only intracrystalline boundaries and is incapable of quantifying any angular orientation variations, unlike the EBSD method that allows identification of both boundaries and orientation variations.

We have also shown that successful application of the EBSD method to alkali-feldspar helps to provide quantitative constraints on the relationship between argon age and orientation microstructure. The complexity of K-feldspar orientation variations even within undeformed granitic feldspars, suggests that a literal interpretation of a simple domain structure, as predicted by the MDD model, appears unlikely (see also Reddy et al., 2001). However, we are able to recognize different sized microstructural domains that appear to record at least a first order relationship with  $^{40}\text{Ar}/^{39}\text{Ar}$  age. The clear relationship between: (1) the largest microstructural “domains” and the oldest  $^{40}\text{Ar}/^{39}\text{Ar}$  apparent ages; and (2) much smaller “domains” and much younger  $^{40}\text{Ar}/^{39}\text{Ar}$  apparent ages, suggests that diffusion from different sized orientation domains is the main control on argon loss in K-feldspar from the Dead Fox Granite. These results are consistent with a microstructural control on multidomain diffusion and hence provide a link between the disparate views of Parsons et al. (1999) and Lovera et al. (1989).

Grain mosaic K-feldspars associated with myrmekitization in the Dead Fox Granite provide a clear candidate group for small to intermediate domains and have  $^{40}\text{Ar}/^{39}\text{Ar}$  ages corresponding to the young ages recorded in the age spectrum. Fitz Gerald and Harrison (1993) were unable to find a candidate for these small to intermediate domains in K-feldspar MH10. Our result is significant in possibly representing the first identification of candidate domains for this size range, corresponding to model Domain C (Table 3). We also recognize clear candidate groups for the largest domain size, which record ages equivalent to the oldest ages in the age spectrum (Fig. 9). These large domains may correspond to modeled Domain F (Table 3). The relative dimensions of modeled Domains C and F vary by a factor of  $\sim 17$  (Table 3) closely matching the relative dimensions of the candidate K-feldspars identified by the microstructural analysis, at around 20–50  $\mu\text{m}$  and around 350–1000  $\mu\text{m}$  respectively. Further work, involving microstructural ‘mapping’ of much larger areas granite is required to investigate this apparent correlation.

The role of sub-micron features has been emphasized by Parsons et al. (1999). However, variations in the abundance and/or argon retention properties of sub-micron features cannot explain the observed variations in  $^{40}\text{Ar}/^{39}\text{Ar}$  apparent age reported here. Unfortunately, limitations on the resolution of in situ  $^{40}\text{Ar}/^{39}\text{Ar}$  dating mean that the ages of sub-micron scale microstructures cannot be constrained by this, or any other study, without significant advances in analytical technique. A key point however, is that if sub-micron scale microstructures are found throughout all feldspars at every scale (Parsons et al., 1999), then their effect on the distribution of argon must be essentially uniform. Thus, such features cannot explain argon heterogeneity within or between K-feldspar grains at the scale of laser Ar analyses unless dislocations and low-angle boundaries are responsible for the heterogeneous distribution of these sub-micron features. This possibility has not yet been investigated. Simple microstructural observations are likely to provide the most useful information on the nature and quality of the thermochronologic information available from any given sample, and microstructural examination should be an essential part of  $^{40}\text{Ar}/^{39}\text{Ar}$  analysis. Recrystallization and/or textural modification, which have been shown to affect the distribution of argon, can generally be recognized using optical or conventional scanning electron microscopy. For such samples proceeding to infer the precise form of the cooling history via the MDD model cannot be recommended. Moreover, the wide range in ages recorded by spot analyses of individual K-feldspars in this study suggests that furnace step-heating, rather than laser ablation  $^{40}\text{Ar}/^{39}\text{Ar}$  analysis, is most appropriate for routine age determinations of K-feldspar.

### Acknowledgments

Geoff Fraser, John Fitz Gerald, Jim Dunlap and Mark Harrison are thanked for helpful discussions throughout the project. Geoff Fraser is also thanked for providing the Dead Fox Granite sample. Oscar Lovera provided initial assistance with the MDD modeling. We are grateful to Ian Parsons for his detailed comments on an earlier version of this manuscript. We are also grateful to Jo Wartho for assistance and guidance with UV  $^{40}\text{Ar}/^{39}\text{Ar}$  analysis. Nick Timms and Rob Hough are thanked for help with sample preparation and Elaine Miller is thanked for assistance with SEM operation. Irradiation of the Dead Fox Granite K-feldspar grain separate was undertaken by the Australian Nuclear Science and Technology Organization, through the Australian Institute of Nuclear Science and Engineering and was analysed at the Research School of Earth Sciences. The ultra-violet laser ablation microprobe  $^{40}\text{Ar}/^{39}\text{Ar}$  analyses were undertaken at the Western Australian Argon Isotope Facility, operated by a consortium consisting of Curtin University and the University of Western Australia. We are grateful to Mark Pearce and an anonymous reviewer for their comments on the manuscript, and Tom Blenkinsop for his editorial efforts. SM acknowledges support of Australian Research Council Australian Postdoctoral Fellowship and Discovery Grant DP0208837 and the University of Melbourne Faculty of Science Centenary Research Fellowship for support during publication. SMR acknowledges a Curtin University Targeted Research Fellowship and ARC Discovery Project DP0664078. This paper is TIGeR contribution 116.

### Appendix A. Supplementary data

Supplementary data associated with this article can be found in the online version, at doi:10.1016/j.jsg.2008.05.008.

### Appendix – $^{40}\text{Ar}/^{39}\text{Ar}$ analytical procedures

A K-feldspar mineral separate (sized between 300 and 450  $\mu\text{m}$ ) from the Dead Fox Granite sample was obtained using routine heavy

liquid flotation and magnetic methods. The sample was concentrated to better than 99% purity with the principal impurities being mineral and fluid inclusions. The sample was irradiated for 672 h in facility X33 (or X34) of the Australian Nuclear Science and Technology Organization HIFAR reactor, Lucas Heights, NSW, Australia. The K-feldspar was packed in an aluminum can with a number of samples of the fluence monitor GA1550 biotite (with K/Ar age 98.79 Ma, McDougall and Roksandic, 1974; Renne et al., 1998). The sample can was inverted 180° three times during the irradiation to minimize the effect of the large neutron flux gradient along the length of the can and a cadmium liner was used to minimize interference from thermal neutrons. The sample was analysed at the Australian National University. During the step-heating experiment the temperature was monitored using a thermocouple at the base of a tantalum crucible within a double-vacuum resistance furnace. The heating schedule comprised a series of 43 steps at temperatures between 450 and 1450 °C (including many duplicate and triplicate isothermal steps; Supplementary Data Table 1). After each heating step, the gas released was exposed to Zr–Al getters for ~10 min to remove all active gases. Purified argon was analysed using a VG Isotech MM3600 gas source mass spectrometer. Measurement was made using a Daly collector and photomultiplier with overall sensitivity of  $3.5 \times 10^{-17}$  mol/mV. Corrections for argon produced by interactions of neutrons with K and Ca were made (Tetley et al., 1980). The  $^{40}\text{K}$  abundance and decay constants were taken from standard values recommended by the IUGS Subcommittee on Geochronology (Steiger and Jäger, 1977).

In situ  $^{40}\text{Ar}/^{39}\text{Ar}$  analysis was undertaken at the Western Australian Argon Isotope facility, part of the John de Laeter Centre for Mass Spectrometry, at Curtin University operated by a consortium consisting of Curtin University and The University of Western Australia. Samples, that had previously been characterized using electron backscatter diffraction, were analysed in situ in thin section. The polished thick sections (~300  $\mu\text{m}$  thickness) were removed from their glass slides and cleaned using ultrasonic treatment in methanol and subsequently deionized water. Regions of interest around  $10 \times 10$  mm were broken off the polished section, individually wrapped in aluminum foil and loaded into an aluminum canister. Biotite age standard Tinto B (K–Ar age of  $409.24 \pm 0.71$  Ma; Rex and Guise, 1995) was loaded at 5 mm intervals along the package to monitor the neutron flux gradient. The package was Cd-shielded and irradiated in the 5C position of the McMaster University Nuclear Reactor, Hamilton, Canada for 89 h. Upon return of the material to Curtin University, the samples were loaded into an ultra-high vacuum laser chamber with a Suprasil 2 viewport and baked to 120 °C overnight to remove adsorbed atmospheric argon from the samples and chamber walls.

Material was ablated using a New Wave Research LUV 213X 4 mJ pulsed quintupled Nd-YAG laser ( $\lambda = 213$  nm) with a variable spot size of 20–350  $\mu\text{m}$ , and a repetition rate of 10 Hz. The laser was fired through a Merchantek computer-controlled x–y–z sample chamber stage and microscope system, fitted with a high-resolution CCD camera, 6 $\times$  computer controlled zoom, high magnification objective lens, and two light sources for sample illumination. Samples were ablated for approximately 10 s and the gases released were 'gettered' using three SAES AP10 getter pumps to remove all active gases. Remaining noble gases were equilibrated into a high sensitivity mass spectrometer (MAP 215-50) operated at a resolution of 600 and fitted with a Balzers SEV 217 multiplier. The automated extraction and data acquisition system was computer controlled, using a LabView program. The mean 3 min extraction system blank Ar isotope measurements (appropriate for spot analyses) obtained during the experiments were  $1.56 \times 10^{-12}$ ,  $1.26 \times 10^{-14}$ ,  $3.38 \times 10^{-15}$ ,  $4.87 \times 10^{-14}$  and  $1.83 \times 10^{-14}$   $\text{cm}^3$  STP for  $^{40}\text{Ar}$ ,  $^{39}\text{Ar}$ ,  $^{38}\text{Ar}$ ,  $^{37}\text{Ar}$  and  $^{36}\text{Ar}$  respectively. Samples were corrected for mass spectrometer discrimination and nuclear interference reactions. Errors quoted on

the ages are 1 sigma.  $^{40}\text{Ar}/^{39}\text{Ar}$  ages were calculated using the decay constants of Steiger and Jäger (1977).

## References

- Bestmann, M., Prior, D.J., 2003. Intragranular dynamic recrystallization in naturally deformed calcite marble: diffusion accommodated grain boundary sliding as a result of subgrain rotation recrystallization. *Journal of Structural Geology* 25, 1597–1613.
- Budd, A.R., Wyborn, L.A.I., Bastrakova, I.V., 2001. The Metallogenic Potential of Australian Proterozoic Granites. *Geoscience Australia Record* 2001/12, 152 pp., ISBN: 0642466904.
- Burgess, R., Kelley, S.P., Parsons, I., Walker, F.D.L., Worden, R.H., 1992.  $^{40}\text{Ar}/^{39}\text{Ar}$  analysis of Perthite microtextures and fluid inclusions in alkali feldspars from the Klokken Syenite, South Greenland. *Earth and Planetary Science Letters* 109, 147–167.
- Castle, R.O., Lindsley, D.H., 1993. An exsolution silica-pump model for the origin of myrmekite. *Contributions to Mineralogy and Petrology* 115, 58–65.
- Chichagov, A.V., Varlamov, D.A., Dilanyan, R.A., Dokina, T.N., Drozhzhina, N.A., Samokhvalova, O.L., Ushakovskaya, T.V., 2001. MINCRYST: a crystallographic database for minerals, local and network (WWW) versions. *Crystallography Reports* 46, 876–879.
- Corsetti, F.A., Stewart, J.H., Hagadorn, J.W., 2006. Neoproterozoic diamicite-cap carbonate succession and  $\delta^{13}\text{C}$  chemostratigraphy from eastern Sonora, Mexico. *Chemical Geology* 237, 129–142.
- Dunlap, W.J., Fossen, H., 1998. Early Paleozoic orogenic collapse, tectonic stability, and late Paleozoic continental rifting revealed through thermochronology of K-feldspars, southern Norway. *Tectonics* 17, 604–620.
- Elkins, L.T., Grove, T.L., 1990. Ternary feldspar experiments and thermodynamic models. *American Mineralogist* 75, 544–559.
- Faul, U.H., Fitz Gerald, J.D., 1999. Grain misorientations in partially molten olivine aggregates: an electron back scattered diffraction study. *Physics and Chemistry of Minerals* 26, 187–197.
- Fitz Gerald, J.D., Harrison, T.M., 1993. Argon diffusion domains in K-feldspar I: microstructures in MH-10. *Contributions to Mineralogy and Petrology* 113, 367–380.
- Fitz Gerald, J.D., Parsons, I., Cayzer, N., 2006. Nanotunnels and pull-aparts: defects of exsolution lamellae in alkali feldspars. *American Mineralogist* 91, 772–783.
- Gatehouse, C.G., Fanning, C.M., Flint, R.B., 1995. Geochronology of the Big Lake Suite, Warburton Basin, northeastern South Australia. *Quarterly Geological Notes of the Geological Survey of South Australia* 128, 8–16.
- Hand, M., Buick, I., 2001. Tectonic evolution of the Reynolds-Anmatjira ranges: a case study in terrain reworking from the Arunta Inlier, central Australia. *Special Publications of the Geological Society of London* 184, 237–260.
- Harrison, T.M., Heizler, M.T., Lovera, O.M., Chen, W., Grove, M., 1994. A chlorine-disinfectant for excess argon released from K-feldspar during step-heating. *Earth and Planetary Science Letters* 123, 95–104.
- Hippert, J.F., Valarelli, J.V., 1998. Myrmekite: constraints on the available models and a new hypothesis for its formation. *European Journal of Mineralogy* 10, 317–331.
- Hough, P.V.C., 1962. Method and Means for Recognizing Complex Patterns. – U.S. Patent, 3069354.
- Jiang, Z., Prior, D.J., Wheeler, J., 2000. Albite crystallographic preferred orientation and grain misorientation distribution in a low-grade mylonite: implications for granular flow. *Journal of Structural Geology* 22, 1663–1674.
- Lee, J.K.W., 1995. Multipath diffusion in geochronology. *Contributions to Mineralogy and Petrology* 120, 60–82.
- Lindsay, J.F., 1989. Depositional controls on glacial facies associations in a basinal setting, late Proterozoic, Amadeus Basin, central Australia. *Palaeogeography, Palaeoclimatology, Palaeoecology* 73, 205–232.
- Lovera, O.M., Richter, F.M., Harrison, T.M., 1989. The  $^{40}\text{Ar}/^{39}\text{Ar}$  thermochronometry for slowly cooled samples having a distribution of diffusion domain sizes. *Journal of Geophysical Research* 94, 17917–17935.
- Lovera, O.M., Richter, F.M., Harrison, T.M., 1991. Diffusion domains determined from  $^{39}\text{Ar}$  released during step-heating. *Journal of Geophysical Research* 96, 2057–2069.
- Lovera, O.M., Grove, M., Harrison, T.M., Mahon, K.I., 1997. Systematic analysis of K-feldspar  $^{40}\text{Ar}/^{39}\text{Ar}$  step heating results: I. Significance of activation energy determinations. *Geochimica et Cosmochimica Acta* 61, 3171–3192.
- Lovera, O.M., Grove, M., Harrison, T.M., 2002. Systematic analysis of K-feldspar  $^{40}\text{Ar}/^{39}\text{Ar}$  step heating results II: relevance of laboratory argon diffusion properties to nature. *Geochimica et Cosmochimica Acta* 66 (7), 1237–1255.
- McDougall, I., 1985. K-Ar and  $^{40}\text{Ar}/^{39}\text{Ar}$  dating of the hominid-bearing Pliocene-Pleistocene sequence at Koobi Fora, Lake Turkana, northern Kenya. *Geological Society of America Bulletin* 96, 159–175.
- McDougall, I., Roksandic, Z., 1974. Total fusion  $^{40}\text{Ar}/^{39}\text{Ar}$  ages using HIFAR reactor. *Journal of the Geological Society of Australia* 21, 81–89.
- McLaren, S., Dunlap, W.J., 2006. The use of  $^{40}\text{Ar}/^{39}\text{Ar}$  K-feldspar thermochronology in basin thermal history reconstruction: an example from the Big Lake Suite granites, Warburton Basin, South Australia. *Basin Research* 18, 189–203, doi:10.1111/j.1365-2117.2006.00288.x.
- McLaren, S., Dunlap, W.J., Sandiford, M., McDougall, I., 2002. Thermochronology of high heat producing crust at Mount Painter, South Australia: implications for tectonic reactivation of continental interiors. *Tectonics* 21, 4, doi:10.1029/2000TC001275.
- Mulch, A., Cosca, M.A., Handy, M.R., 2002. In-situ UV-laser  $^{40}\text{Ar}/^{39}\text{Ar}$  geochronology of a micaceous mylonite: an example of defect-enhanced argon loss. *Contributions to Mineralogy and Petrology* 142, 738–752.
- Page, R., 1996. Sample 2000082040. Unpublished data in Geoscience Australia OZCHRON geochronology database. <http://www.ga.gov.au>.
- Parsons, I., Brown, W.L., 1984. Feldspars and the thermal history of igneous rocks. In: Brown, W.L. (Ed.), *Feldspars and Feldspathoids: Structure, Properties and Occurrences*. NATO ASI Series C. Reidel Publishing, Dordrecht, pp. 317–371.
- Parsons, I., Brown, W.L., Smith, J.V., 1999.  $^{40}\text{Ar}/^{39}\text{Ar}$  thermochronology using alkali feldspars: real thermal history or mathematical mirage of microtexture? *Contributions to Mineralogy and Petrology* 136, 92–110.
- Prince, E., Donnay, G., Martin, R.F., 1973. Neutron diffraction refinement of an ordered orthoclase structure. *American Mineralogist* 58, 500–509.
- Prior, D.J., Wheeler, J., 1999. Feldspar fabrics in a greenschist facies albite-rich mylonite from electron backscatter diffraction. *Tectonophysics* 303, 29–49.
- Prior, D.J., Trimby, P.W., Weber, U.D., 1996. Orientation contrast imaging of microstructures in rocks using focusscatter detectors in the scanning electron microscope. *Mineralogical Magazine* 60, 859–869.
- Prior, D.J., Boyle, A.P., Brenker, F., Cheadle, M.C., Day, A., Lopez, G., Peruzzo, L., Potts, G.J., Reddy, S., Spiess, R., Timms, N.E., Trimby, P., Wheeler, J., Zetterström, L., 1999. The application of electron backscatter diffraction and orientation contrast imaging in the SEM to textural problems in rocks. *American Mineralogist* 84, 1741–1759.
- Prior, D.J., Wheeler, J., Peruzzo, L., Spiess, R., Storey, C., 2002. Some garnet microstructures; an illustration of the effect of orientation maps and misorientation analysis in microstructural studies. *Journal of Structural Geology* 24, 999–1011.
- Randle, V., 2000. Theoretical framework for electron backscatter diffraction. In: Swartz, A.J., Kumar, M., Adams, B.L. (Eds.), *Electron Backscatter Diffraction in Materials Science*. Kluwer Academic, New York, pp. 19–30.
- Reddy, S.M., Potts, G.J., Kelley, S.P., Arnaud, N.O., 1999. The effects of deformation-induced microstructures on intragrain  $^{40}\text{Ar}/^{39}\text{Ar}$  ages in potassium feldspar. *Geology* 27, 363–366.
- Reddy, S.M., Potts, G.J., Kelley, S.P., 2001.  $^{40}\text{Ar}/^{39}\text{Ar}$  ages in deformed potassium feldspar: evidence of microstructural control on Ar isotope systematics. *Contributions to Mineralogy and Petrology* 141, 186–200.
- Reddy, S.M., Timms, N.E., Pantleon, W., Trimby, P., 2007. Quantitative characterization of plastic deformation of zircon and geological implications. *Contributions to Mineralogy and Petrology* 153, 625–645.
- Reddy, S.M., Timms, N.E., Eglinton, B.M., 2008. Electron backscatter diffraction analysis of zircon: a systematic assessment of match unit characteristics and pattern indexing optimization. *American Mineralogist* 93, 187–197.
- Renne, P.R., Swisher, C.C., Deino, A.L., Karner, D.B., Owens, T.L., DePaolo, D.J., 1998. Intercalibration of standards, absolute ages and uncertainties in  $^{40}\text{Ar}/^{39}\text{Ar}$  dating. *Chemical Geology* 145, 117–152.
- Rex, D.C., Guise, P.G., 1995. Evaluation of argon standards with special emphasis on time scale measurement. In: Odin, G.S. (Ed.), *Phanerozoic Time Scale*. Bull. Liaison Inform. IUGS Subcommission Geochronology, vol. 13, pp. 21–23.
- Richter, F.M., Lovera, O.M., Harrison, T.M., Copeland, P., 1991. Tibetan tectonics from  $^{40}\text{Ar}/^{39}\text{Ar}$  analysis of a single K-feldspar sample. *Earth and Planetary Science Letters* 105, 266–278.
- Skrotzki, W., Tamm, R., Oertel, C.-G., Roseberg, J., Brokmeier, H.-G., 2000. Microstructure and texture formation in extruded lead sulfide (galena). *Journal of Structural Geology* 22, 1621–1632.
- Spell, T.L., McDougall, I., Dougeris, A.P., 1996. Cerro Toledo Rhyolite, Jemez Volcanic Field, New Mexico:  $^{40}\text{Ar}/^{39}\text{Ar}$  geochronology of eruptions between two caldera-filling events. *Geological Society of America Bulletin* 108, 1549–1566.
- Steiger, R., Jäger, E., 1977. Subcommission on geochronology: convention on the use of decay constants in geo- and cosmochronology. *Earth and Planetary Science Letters* 36, 359–362.
- Sun, X., 1997. Structural style of the Warburton Basin and control in the Cooper and Eromanga Basins, South Australia. *Exploration Geophysics* 28, 333–339.
- Swisher III, C.C., Dungs, L., Butler, R.F., 1993.  $^{40}\text{Ar}/^{39}\text{Ar}$  dating and magnetostratigraphic correlation of the terrestrial Cretaceous-Paleogene boundary and Puerca Mammal Age, Hell Creek-Tullock formations, eastern Montana. *Canadian Journal of Earth Sciences* 30, 1981–1996.
- Tetley, N., McDougall, I., Heydegger, H.R., 1980. Thermal neutron interferences in the  $^{40}\text{Ar}/^{39}\text{Ar}$  dating technique. *Journal of Geophysical Research* 85, 7201–7205.
- Teysier, C., Amri, C., Hobbs, B.E., 1988. South Arunta Block: the internal zones of a Proterozoic overthrust in central Australia. *Precambrian Research* 40/41, 157–173.
- Waldron, K., Lee, M.R., Parsons, I., 1994. The microstructures of perthitic alkali-feldspars revealed by hydrofluoric acid etching. *Contributions to Mineralogy and Petrology* 116, 360–364.
- Walter, M.R., Veivers, J.J., Calver, C.R., Grey, K., 1995. Neoproterozoic stratigraphy of the Centralian Superbasin, Australia. *Precambrian Research* 73, 173–195.
- Wartho, J.-A., Kelley, S.P., Booker, R.A., Carroll, M.R., Villa, I.M., Lee, M.R., 1999. Direct measurement of Ar diffusion profiles in a gem-quality Madagascar K-feldspar using the ultra-violet laser ablation microprobe (UVALMP). *Earth and Planetary Science Letters* 170, 141–153.
- William, C., Brown, W.L., 1974. A coherent elastic model for the determination of the orientation of exsolution boundaries: application to feldspars. *Acta Crystallographica* 30, 316–331.
- Winter, J.K., Okamura, F.P., Ghose, S., 1979. A high-temperature structural study of high albite, monalbite, and the analbite – monalbite phase transition. *American Mineralogist* 64, 409–423.
- Zhao, J.-X., McCulloch, M.T., 1993. Sm-Nd mineral isochron ages of late Proterozoic dyke swarms in Australia; evidence for two distinctive events of mafic magmatism and crustal extension. *Chemical Geology* 109, 341–354.